J Solid State Electrochem (2012) 16:1823–1832
DOI 10.1007/s10008-012-1662-2

ORIGINAL PAPER

Li-cycling properties of nano-crystalline $(Ni_{1-x}Zn_x)Fe_2O_4$ $(0 \le x \le 1)$

Christie Thomas Cherian · M. V. Reddy · G. V. Subba Rao · Chorng Haur Sow · B. V. R. Chowdari

Received: 11 August 2011 / Accepted: 21 January 2012 / Published online: 28 February 2012

Abstract Sol–gel auto-combustion method is adopted to prepare solid solutions of nano-crystalline spinel oxides, $(Ni_{1-x}Zn_x)Fe_2O_4$ $(0 \le x \le 1)$.The phases are characterized by X-ray diffraction (XRD), high-resolution transmission electron microscopy, selected area electron diffraction, and Brunauer–Emmett–Teller surface area. The cubic lattice parameters, calculated by Rietveld refinement of XRD data by taking in to account the cationic distribution and affinity of Zn ions to tetrahedral sites, show almost Vegard's law behavior. Galvanostatic cycling of the heat-treated electrodes of various compositions are carried in the voltage range 0.005–3 V vs. Li at 50 mAg^{-1} up to 50 cycles. Phases with high Zn content $x \ge 0.6$ showed initial two-phase Li-intercalation in to the structure. Second-cycle discharge capacities above 1,000 mAh g^{-1} are observed for all x. However, drastic capacity fading occurs in all cases up to 10–15 cycles. The capacity fading between 10 and 50 cycles is found to be greater than 52% for $x \le 0.4$ and for $x=0.8$. For $x=0.6$ and $x=1$, the respective values are 40% and 18% and a capacity of 570 and 835 mAh g^{-1} is retained after 50 cycles. Cyclic voltammetry and ex situ transmission electron microscopy data elucidate the Li-cycling mechanism involving conversion reaction and Li–Zn alloying–dealloying reactions.

Keywords $(Ni_{1-x}Zn_x)Fe_2O_4$ $(0 \le x \le 1)$ · Anodes: Li-cycling properties

C. T. Cherian · M. V. Reddy · G. V. S. Rao · C. H. Sow · B. V. R. Chowdari (✉)
Department of Physics, National University of Singapore, Singapore 117542, Singapore
e-mail: phychowd@nus.edu.sg

Introduction

Lithium ion batteries (LIBs) have become the preferred power source for hand-held devices due to their small size and light weight [1]. Desired characteristics for negative electrode (anode) materials of LIBs include large reversible specific capacity with less initial capacity loss, low voltage profile vs. Li-metal, good Li-ion kinetics, compatibility with electrolyte and binder systems, low cost, environmental-friendly, and long cycle life and calendar life [1]. A wide variety of binary and ternary oxides have been studied as prospective anode materials for Li-ion batteries which undergo Li-cycling via the "conversion reaction," and those have been recently reviewed by Cabana et al. [2]. Iron-based spinel oxides such as Fe_3O_4 [3], ferrites with general formula AFe_2O_4 (A = Zn, Ni, Co, Cu, Cd) [4–8] have been extensively studied for their Li-cyclability. The general composition for the spinel structure is represented as $A[B_2]O_4$ in which the number of B^{3+} ions is twice that of the A^{2+} ions. Normal spinel has a cubic close-packed oxygen array in which A^{2+} ions occupy one eighth of the tetrahedral 8a-sites and B^{3+} ions occupy one half of the octahedral 16 d-sites in the space group, $Fd3m$ [9]. The spinel structure is flexible with regard to the distribution of A and B ions at tetrahedral and octahedral sites. When A ions occupy one half of the octahedral 16(d) sites and B ions occupy the other half of the octahedral 16(d) sites as well as all of the tetrahedral 8(a) sites, namely, (B)[A,B]O_4, the structure is called an inverse spinel, and the degree of inversion is unity [9]. Mixed spinels are those in which the degree of inversion lies between 0 and 1. In the literature, many years ago, Chen et al. [10] studied the room temperature Li-insertion reactions of several cubic iron spinels, MFe_2O_4 with M^{2+}=Mn, Fe, Co, Ni, Cu, Zn, and Cd by using butyl–Li. They found that the

maximum amount of Li ions that may be incorporated in to the ferrites decrease in the order, inverse > "mixed" > normal spinel [10].However, the critical Li-ion concentration (x_c) above which the cubic spinel to rock salt transition occurs is larger for normal spinels than for inverse spinels. That is x_c ~0.5 for $ZnFe_2O_4$ and ~0.1 for Fe_3O_4 [10].

$NiFe_2O_4$ has an inverse spinel structure where the Ni^{2+} and half of Fe^{3+} cations occupy octahedral site and remaining Fe^{3+} occupy the tetrahedral site, $Fe^{3+}[Ni^{2+}, Fe^{3+}]O_4$. It undergoes Li-cycling via conversion reaction with a theoretical capacity of 915 mAh g^{-1}, corresponding to 8 moles of Li. Several efforts have been made to improve the long-term Li-cycling behavior of $NiFe_2O_4$ such as adopting different synthesis methods to control the particle size and morphology and partial substitution of host structure with metal cations. Tirado's group has done extensive work on the Li-cycling properties of $NiFe_2O_4$ and the origin of capacity fading in it, up on cycling [6, 11, 12]. They found that capacity fading occurs in $NiFe_2O_4$ up to 20 cycles irrespective of the preparation conditions, and thereafter, the capacity stabilizes or continues to fade depending on the temperature and/or method of synthesis [11]. Among $NiFe_2O_4$ phases that have been prepared by sol–gel method, those annealed at 1000 °C showed good capacity retention, namely 550 mAh g^{-1} and was observed after 50 cycles at 1 C-rate. The authors concluded that mutually interconnected sub-micron particles that defines a macroporous system is essential to sustain high capacity values over a large number of cycles [11].

Lavela et al. [13] partially substituted Fe^{3+} with Mn^{3+} in $NiFe_2O_4$ nanoparticles and studied its electrochemical performance. Capacities close to 800 mAh g^{-1} after 40 cycles and 750 mAh g^{-1} after 50 cycles were obtained for $NiMnFeO_4$ and $NiFe_2O_4$, respectively. Zhao et al. [14] prepared nano-sized $NiFe_2O_4$ (5–15 nm) with high surface area by hydrothermal method at 230 °C and found that the first discharge capacity reached a value of 1,314 mAh g^{-1}. But the discharge capacity decreased to 791 and 709.0 mAh g^{-1} at a current density of 0.2 mA cm^{-2} after two and three cycles, respectively. Recently, Zhao et al. [15] prepared $NiFe_2O_4$/SWNT (single-walled carbon nanotubes) composite with a loading ratio of 70 wt.% by hydrothermal method and studied the Li-cycling properties. They reported that a reversible capacity of 776 mAh g^{-1} was retained after 55 cycles when cycled in the range of 0.005–3.0 V at a current density of 150 mAg^{-1}. $NiFe_2O_4$ nanoparticles (5 nm) were homogeneously anchored on the surface of the SWNTs, and the excellent electrochemical performance of the composite was attributed to the synergistic effect between SWNT and $NiFe_2O_4$. Thus, apart from the nano-size, inter-particle connectivity is also an important factor affecting the cycling stability of $NiFe_2O_4$.

Zinc ferrite, $ZnFe_2O_4$, is a normal spinel where only the Zn-ions occupy the tetrahedral site, $Zn^{2+}[Fe_2^{3+}]O_4$. Guo et al. [4] recently showed that well-dispersed hollow spheres composed of 10–20 nm $ZnFe_2O_4$ nanoparticles deliver high reversible capacity of 900 mAh g^{-1} and show good cycling stability and current (C) rate performance. This can be compared with the theoretical capacity of 1,000 mAh g^{-1}. Zn has been proven to be a good matrix element for conversion-based electrodes such as $ZnCo_2O_4$ and $ZnMn_2O_4$ since it can contribute additional capacity due to alloying-de-alloying reaction besides buffering the volume variation during conversion reaction [4, 5, 16, 17]. It is also known that the capacity stability of conversion–reaction-based electrodes depends on the initial crystal structure which determines the local environment of the participating ions during Li-cycling [16, 18]. So it is of interest to study the effect of doping $NiFe_2O_4$ with varying amounts of Zn and the consequent cation redistribution, on the Li-cycling behavior. Presently, we describe the preparation of nano-size solid solutions, $(Ni_{1-x}Zn_x)Fe_2O_4$, and their Li-cycling behavior.

Experimental

The solid solutions, $(Ni_{1-x}Zn_x)Fe_2O_4$ (x=0, 0.2, 0.4, 0.6, 0.8, 1) were prepared by citrate gel auto combustion method reported by Hankare et al. [19]. Citric acid (Sigma Aldrich, 99.5%), zinc nitrate hexahydrate (Sigma Aldrich, 98%), nickel nitrate hexahydrate (Fluka, 98%), and ferric citrate hydrate (Merck, 98%) are used as starting materials. Zinc nitrate and nickel nitrate solutions, of required concentrations, are prepared and kept in separate beakers. Citric acid solution is prepared and added to the above solutions. A clear transparent solution of metal–citrate complex is obtained. The resultant solutions are added to iron citrate solution with constant stirring. The mixture was evaporated on hot plate slowly to obtain a porous mass. The compositions with varying x were heated at 700 °C for 5 h in air. The compounds, ~4 g for each x, were characterized by powder X-ray diffraction (XRD) (Philips X'PERT MPD, Cu K_α and the data were refined using TOPAS software, R 2.1 version) and high-resolution transmission electron microscope (HRTEM) (JEOL JEM 2100 operating at 200 kV). Brunauer–Emmett–Teller (BET) surface areas were determined from results of N_2 physisorption at 77 K using Tristar 3000 (Micromeritics, USA), and the powder samples were preheated under nitrogen flow for 1 h at 150 °C to remove adsorbed moisture. The Ni and Zn contents are determined by the inductively coupled plasma optical emission spectrometer (Perkin Elmer Dual-View Optima DV) system. Sample dissolution is carried out by Milestone microwave laboratory system, USA, using aqua-regia.

The electrodes for Li-cycling were prepared by the doctor-blade technique using a mixture of the active material ($Ni_{1-x}Zn_xFe_2O_4$), Super P carbon (MMM Ensaco) and binder (Kynar 2801) in the mass ratio 70:15:15, using an etched Cu-foil (thickness 10 μm) as the current collector. All the electrodes were heat-treated in argon atmosphere at 240 °C for 5 h and cooled to ambient temperature. This is to ensure melting and solidification of the binder and uniform distribution of the active mass on the electrode. Coin-type test cells (size 2016) were assembled using Li metal as counter electrode, glass micro-fiber filter as the separator, and 1 M $LiPF_6$ in ethylene carbonate and dimethyl carbonate (1:1 by volume) as the electrolyte. Galvanostatic discharge–charge cycling and cyclic voltammetry of the cells were carried out at room temperature (25 °C) by computer-controlled battery tester (model SCN, Bitrode, USA) and Macpile II (Biologic, France), respectively. Details of electrode preparation, coin cell fabrication, and sample handling for TEM are discussed elsewhere [20].

Results and discussion

Crystal structure and morphology

The as-prepared compounds vary in color from dark brown to yellow with increasing Zn content. The powder XRD patterns of the compositions of ($Ni_{1-x}Zn_x$) Fe_2O_4, x=0, 0.2, 0.4, 0.6, 0.8, 1 are shown in Fig. 1, and they revealed the formation of compound in phase pure form with the cubic spinel structure without any impurities. The lattice parameter values (a) are obtained by the Rietveld refinement and are in good agreement with reported values of $NiFe_2O_4$ (JCPDS 86–2267) and $ZnFe_2O_4$ (JCPDS 82–1049). The variation of lattice parameter with the Zn concentration is given in Table 1 along with the Rietveld parameters. Since Zn^{2+} always prefers to occupy tetrahedral site, doping of Zn^{2+} in to $NiFe_2O_4$ displaces equal amount of Fe^{3+} from the tetrahedral site and the displaced Fe^{3+} occupy the octahedral sites of Ni^{2+} [19]. The cationic distribution at the tetrahedral site and octahedral site with varying x has been determined from the magnetization data by Hankare et al. [19]. Thus, we can expect a gradual linear increase in the lattice parameter with the increase in zinc content, since the ionic radius of Zn^{2+} (tetrahedral coordination, 0.60 Å) is greater than that of Fe^{3+} (tetrahedral coordination, 0.49 Å) [21]. On the other hand, replacement of Ni^{2+} (r_i, octahedral coordination, 0.69 Å) by Fe^{3+} (r_i, octahedral coordination, 0.645 Å) produces only marginal decrease in the average ionic radius. The observed a values in the present study are in good agreement with those reported by Hankare et al. [19] and almost obeys the Vegard's law.

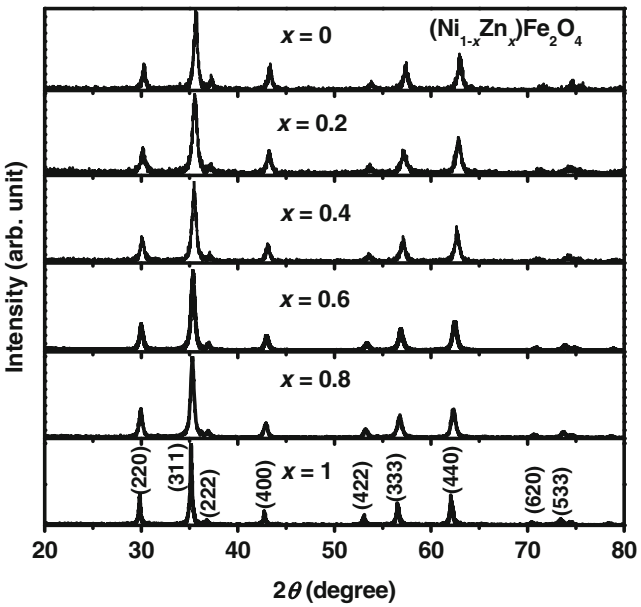

Fig. 1 X-ray diffraction (XRD) patterns of ($Ni_{1-x}Zn_x$) Fe_2O_4, x=0, 0.2, 0.4, 0.6, 0.8, 1. Miller indices are shown. Cu K_α radiation. The y-axis values are normalized for better comparison

The particle morphology was examined by TEM. Figure 2a, b show that the $NiFe_2O_4$ and $ZnFe_2O_4$ powder consists of nanoparticles of size approximately 45 and 25 nm, respectively. Figure 2c, d shows the HRTEM lattice images of $NiFe_2O_4$ and $ZnFe_2O_4$. They show clearly the lattice fringes and the measured inter-planar spacings match well with the d value corresponding to the (111) plane of the XRD patterns of the compounds. Inset in Fig. 2d shows the selected area electron diffraction (SAED) pattern consisting of diffuse rings and bright spots with (220) and (311) planes, indicating nano-phase nature. The particle size of $NiFe_2O_4$ is found to be slightly larger than that of the other compositions due to the high energy barriers for the formations of $NiFe_2O_4$ as compared with that of $ZnFe_2O_4$ [19]. The crystallite sizes of ($Ni_{1-x}Zn_x$)Fe_2O_4 are calculated by the Scherrer's equation from the Rietveld refined data, given in Table 1, and compare very well with the particle size derived from the TEM data on x=0 and 1. The values also compare well with the data reported by Hankare et al. [19]. The BET surface area of the phases was found to be in the range of 32 to 21 $m^2\ g^{-1}$ for various values of x (Table 1). These are typical of mixed oxides prepared at 700 °C. The elemental analysis of ($Ni_{1-x}Zn_x$)Fe_2O_4 phases was carried out and the obtained experimental weight percent of Zn and Ni for various compositions are given in Table 1. As can be seen, the values match fairly well with the calculated values.

Galvanostatic Li-cycling properties

The electrochemical Li-storage and cyclability of all the compositions ($Ni_{1-x}Zn_x$)Fe_2O_4 were investigated by

Table 1 Structure and other data of $(Ni_{1-x}Zn_x)Fe_2O_4$

$(Ni_{1-x}Zn_x)Fe_2O_4$						
x	0	0.2	0.4	0.6	0.8	1
Lattice parameter (a), Å	8.341 (1)	8.355 (4)	8.371 (4)	8.399 (7)	8.422 (3)	8.441 (3)
R_{wp} (weight-profile)	34	36	38	30	30	39
R_B (Rietveld–Bragg)	8.6	7.7	8.7	5.1	4.5	9.1
GOF (goodness of fit)	1.2	1.1	1.2	1.3	1.4	1.1
BET surface area (±0.2 m^2 g^{-1})	31.9	30.1	24.7	20.7	28.1	27.0
Zn wt.%						
Calc.	0	5.6	11.0	16.5	21.8	27.1
Exp.	0	5.6	10.1	16.3	21.0	27.3
Ni wt.%						
Calc.	25.0	19.9	14.8	9.9	4.9	0
Exp.	26.2	19.8	14.7	10.3	6.1	0
Crystallite size, nm (from Scherrer equation)	35	27	25	24	28	22

galvanostatic cycling in the voltage window, 0.005–3.0 V vs. Li at a current of 50 mA g^{-1} up to 50 cycles. Voltage vs. capacity profiles of the selected cycles are shown in Fig. 3. For the compositions, x=0 and 0.2 (Fig. 3a, b), the first discharge curve starts from the open circuit voltage (OCV~2.5–3 V) and shows a continuous decrease, to reach a voltage plateau region at 0.8 V. For x=0, up to the voltage plateau, a capacity of ~190 mAh g^{-1} (~1.7 moles of Li) is obtained due to the single-phase Li-intercalation reaction to give $Li_{\sim 2}NiFe_2O_4$ (Fig. 3a). Using butyl–Li, Chen et al. [10] have shown that $NiFe_2O_4$ spinel can incorporate up to 2 moles of Li without any change in crystal structure. However, they reported that only 0.5 Li can be chemically intercalated in to $ZnFe_2O_4$. For the compositions with

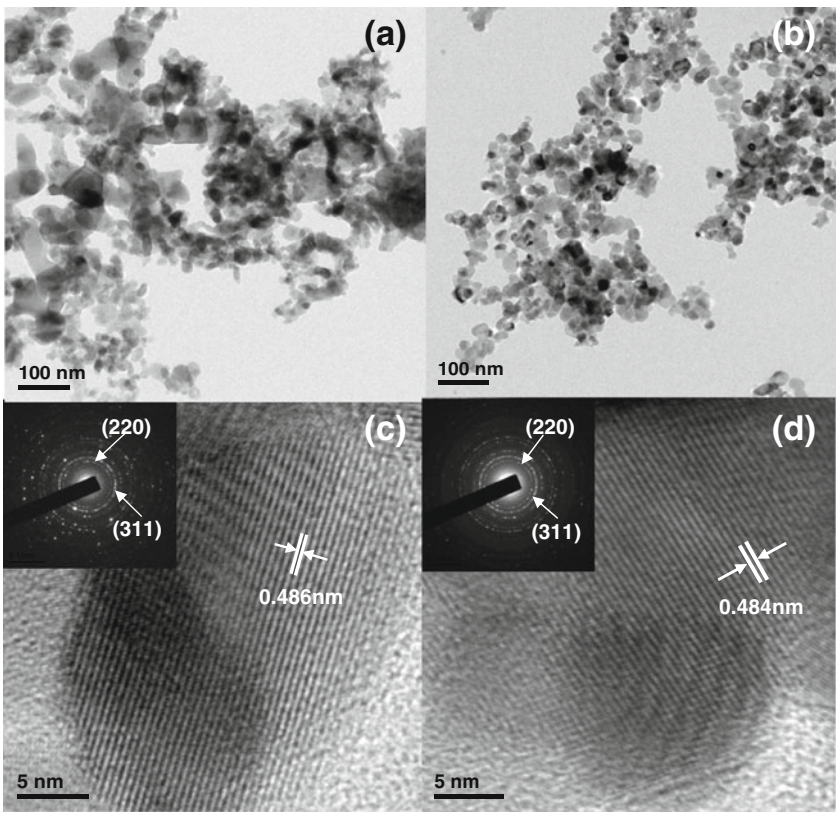

Fig. 2 **a**, **b** TEM photographs of $NiFe_2O_4$ and $ZnFe_2O_4$ showing agglomerates of nanoparticles. Scale *bar* is 100 nm. **c**, **d** HRTEM lattice images of nano-phase $NiFe_2O_4$ and $ZnFe_2O_4$. Scale *bar* is 5 nm. *Inset* in **c** and **d** show the SAED patterns and selected Miller indices

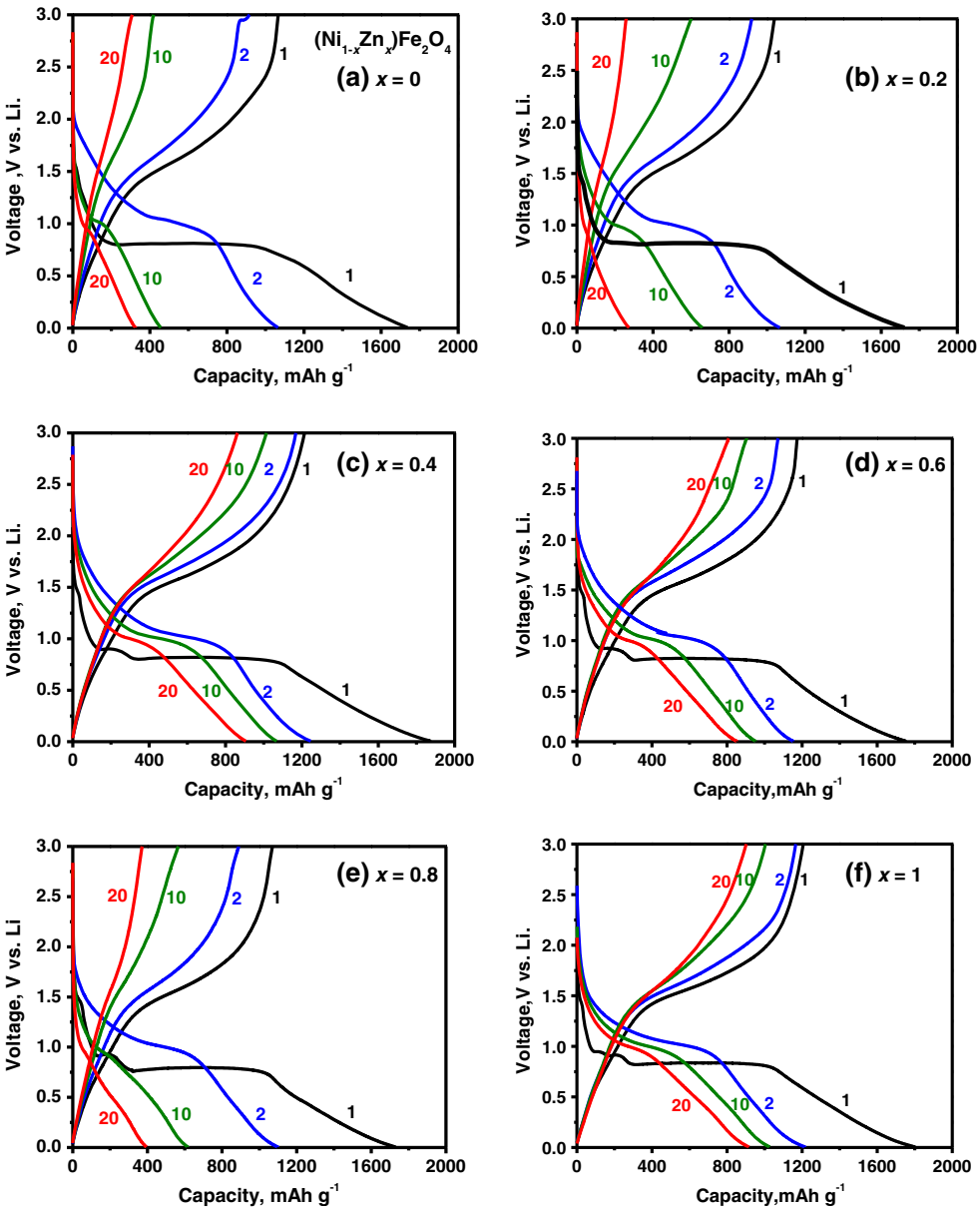

Fig. 3 Voltage vs. capacity profiles of $(Ni_{1-x}Zn_x)Fe_2O_4$. **a** x=0, **b** x=0.2, **c** x=0.4, **d** x=0.6, **e** x=0.8, **f** x=1.0. *Numbers* refer to cycle number. Voltage range, 0.005–3 V vs. Li; current, 50 mAg^{-1}

higher Zn content, x=0.4, 0.6, 0.8, 1, two vivid voltage plateaus are present in addition to the one at 0.8 V, which shows that Li-intercalation takes place as a two-phase reaction (Fig. 3c–f). Two Li-insertion plateaus, one between 0.8 and 1 V and another between 1.3 and 1.5 V, can be clearly seen for $x \geq 0.6$. It is clear from the Fig. 3c–f that, before the onset of voltage plateau near 0.8 V, a capacity of 310–320 mAh g^{-1} is obtained which corresponds to insertion of ~3.5 moles of Li. Guo et al. [4] observed a similar behavior in hollow spheres of nano-$ZnFe_2O_4$ in which two vivid voltage plateaus were seen before 0.8 V when the electrode was first discharged to 0.005 V. Based on XRD studies, the phase composition of the material is recognized to be modified from pristine spinel $ZnFe_2O_4$ to cubic $Li_{0.5}ZnFe_2O_4$ with a=8.455 Å and space group, Fd3m (between OCV and 1.1 V) and then to simple cubic-$Li_2ZnFe_2O_4$ with a=8.463 Å and space group, Fd3m (between 1.1 and 0.8 V) [4, 22]. This behavior is exactly seen in pure $ZnFe_2O_4$ nanoparticles (x=1) which is shown in Fig. 3f and represented by Eqs. 1 and 2 [4, 5, 22]. Guo et al. [4] and Ding et al. [22] have shown that Eqs. 1 and 2 are reversible when cycling is carried out in the range, 1–4.5 V or 0.8–4.5 V vs. Li. However, in the present case, these reactions are not reversible since cycling is carried out in the range 0.005–3.0 V.

Further reaction of Li with the intercalated phase, $Li_x(Ni_{1-x}Zn_x)Fe_2O_4$, leads to crystal structure destruction

and reduction of metal ions followed by the formation of metal nanoparticles embedded in an amorphous matrix of Li_2O and is represented by the large voltage plateau at ~0.8 V (Fig. 3 and Eq. 3).

$$ZnFe_2O_4 + 0.5Li^+ + 0.5e^- \rightarrow Li_{0.5}ZnFe_2O_4 \quad (e = \text{electron}) \quad (1)$$

$$Li_{0.5}ZnFe_2O_4 + 1.5Li^+ + 1.5e^- \rightarrow Li_2ZnFe_2O_4 \quad (2)$$

$$Li_2ZnFe_2O_4 + 6Li^+ + 6e^- \rightarrow 4Li_2O + Zn + 2Fe \quad (3)$$

$$Zn + Li^+ + e^- \rightleftarrows LiZn \quad (4)$$

For the compositions containing Zn, beyond the voltage plateau region, Zn nanoparticles react with Li to form Li–Zn alloy increasing the Li-storage capacity, as per Eq. 4. Guo et al. [4] confirmed the existence on Li–Zn alloy and Fe in the 0.005 V-discharged $ZnFe_2O_4$ from the analysis of SAED pattern and TEM studies of discharged electrodes. Wang et al. [23] reported that Li begins to insert in to metallic zinc at ~0.26 V and the Li–Zn alloy was formed at 0.16 V vs. Li at room temperature. According to Wang et al. [24], during electrochemical reaction of Li with ZnO, Li–Zn alloy formation occurs at 0.35 V and multi-step de-alloying process of Li–Zn alloy occurs in the range 0.1 to 0.8 V. Since the weight percent of Zn in $ZnFe_2O_4$ is only 27%, the Li–Zn alloy formation is not clearly visible in the galvanostatic cycling profiles or in cyclic voltammetry of $ZnFe_2O_4$. However, the additional capacity due to alloying of Zn is clearly seen in the first discharge and second discharge capacities of $Ni_{1-x}Zn_xFe_2O_4$ for x=0 and x=1 given in Table 2. Thus, while $NiFe_2O_4$ shows a second discharge capacity of 1,068 (±10) mAh g^{-1}, the value for $ZnFe_2O_4$ is 1,215 (±10) mAh g^{-1}. In the charging process (Li-extraction), the initial spinel ferrite phase is not recovered, but simpler oxides are formed after the de-alloying reaction of Eq. 4, as per the conversion reactions shown in Eqs. 5, 6, and 8 [4, 5, 22].

$$Zn + Li_2O \rightleftarrows ZnO + 2Li^+ + 2e^- \quad (5)$$

$$2Fe + 3Li_2O \rightleftarrows Fe_2O_3 + 6Li^+ + 6e^- \quad (6)$$

Upon deep discharge to 0.005 V, in the Li-intercalated phase, $Li_{\sim 2}NiFe_2O_4$ undergoes crystal structure destruction and form metal nanoparticles as per Eq. 7. The electrochemically formed Ni and Fe nanoparticles are converted to respective oxides during charging, a reversible process as shown in Eqs. 6 and 8.

$$Li_{\sim 2}NiFe_2O_4 + 6Li^+ + 6e^- \rightarrow Ni + 2Fe + 4Li_2O \quad (7)$$

$$Ni + Li_2O \rightleftarrows NiO + 2Li^+ + 2e^- \quad (8)$$

Figure 4 illustrates the capacity vs. cycle number plots extracted from galvanostatic cycling data. The first, second, tenth, thirtieth, and fiftieth discharge capacity values of all compositions, $(Ni_{1-x}Zn_x)Fe_2O_4$ along with percent capacity-fading are given in the Table 2. It is clear that capacity stability is enhanced with an increase in the Zn-content. The first discharge capacity values vary with x (Zn-content) and are in the range of 1,720–1,875 (±10) mAh g^{-1}. As mentioned earlier, the theoretical reversible capacity of $NiFe_2O_4$ and $ZnFe_2O_4$ and their solid solutions are in the range 914 (x=0)–1,000 (x=1) mAh g^{-1}. In the present study, the observed excess capacity can be explained as due to formation of solid electrolyte interphase (SEI) and an organic polymeric layer on the metal nanoparticles when the electrode potential decreases and approaches 0.005 V. For x=0 and x=0.2, the reversible capacity fades rapidly up to 30 cycles and thereafter reaches 200 and 220 mAh g^{-1}, respectively, after 50 cycles. The behavior of $NiFe_2O_4$ is consistent with the many reports in the literature [6, 11, 12]. An enhancement in the capacity values with increasing Zn concentration is observed for x=0.4 and 0.6. However, capacity-fading is observed for all compositions, the values ranging from 40% to 67% for x=0.2 to 0.8 between 10 and 50 cycles (Table 2 and Fig. 4). The phase with x=0.8 $(Ni_{0.2}Zn_{0.8})Fe_2O_4$ shows a trend in the capacity fading similar to that of x=0 and 0.2, even though it is expected to perform analogous to the phases with x=0.6 and 1 (Figs. 3 and 4 and Table 2).We repeated the synthesis and Li-cycling

Table 2 Discharge capacities at selected cycles for different compositions of $(Ni_{1-x}Zn_x)Fe_2O_4$

Discharge capacity (±10) mAh g^{-1}						
x $(Ni_{1-x}Zn_xFe_2O_4)$	First cycle	Second cycle	Tenth cycle	30th cycle	50th cycle	Capacity-fading (10–50 cycles, %)
0	1,735	1,068	457	275	200	56
0.2	1,722	1,065	660	275	220	67
0.4	1,875	1,244	1,069	715	432	60
0.6	1,755	1,155	947	775	570	40
0.8	1,730	1,110	615	340	294	52
1	1,805	1,215	1,024	880	835	18

Voltage range, 0.005–3 V; current, 50 mAg^{-1}

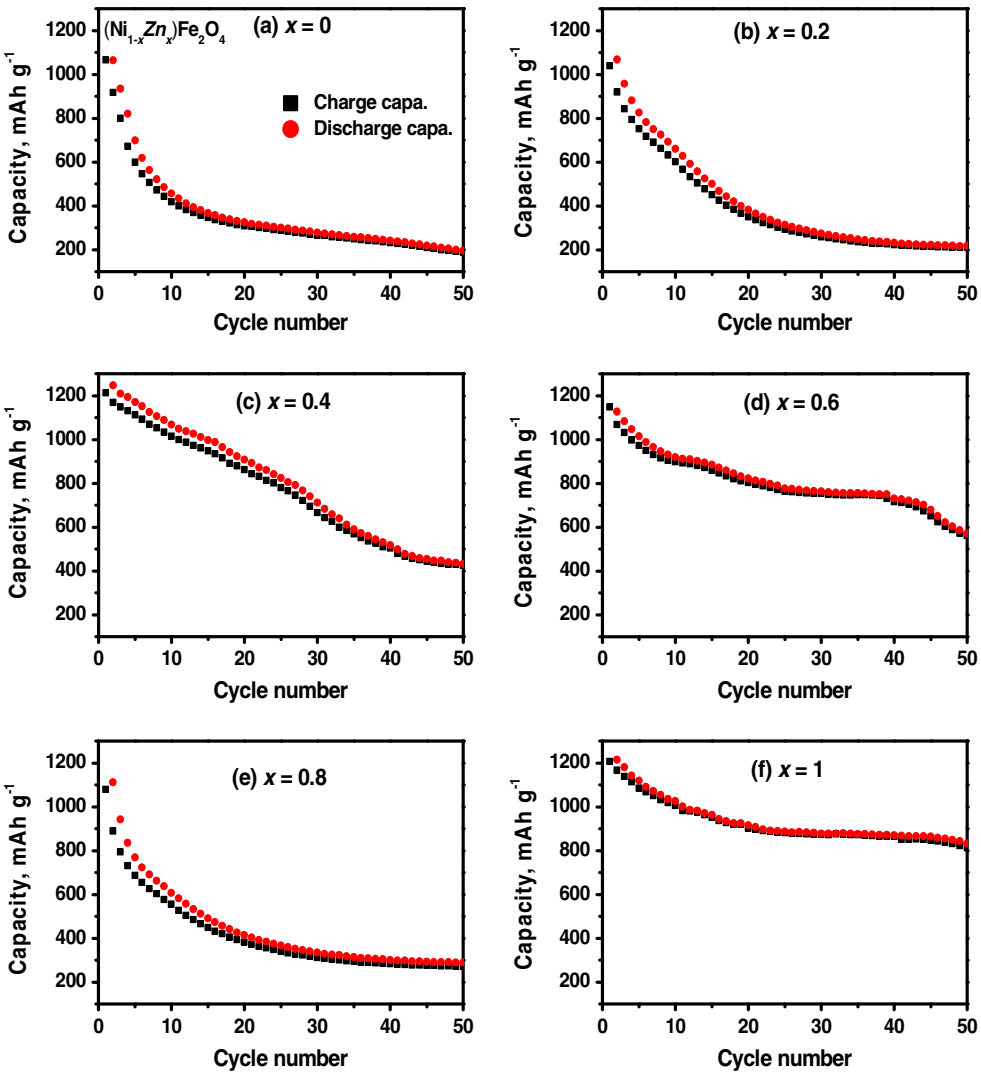

Fig. 4 Capacity vs. cycle number plots for $(Ni_{1-x}Zn_x)Fe_2O_4$. **a** x=0, **b** x=0.2, **c** x=0.4, **d** x=0.6, **e** x=0.8, **f** x=1.0. Voltage range, 0.005–3 V vs. Li; current, 50 mAg^{-1}. First discharge capacity values are not shown

experiments on this phase (x=0.8), and the results are reproducible with in 5–10% with regard to the capacity values and their variations with the cycle number. The reason for this peculiar behavior is not known at present.

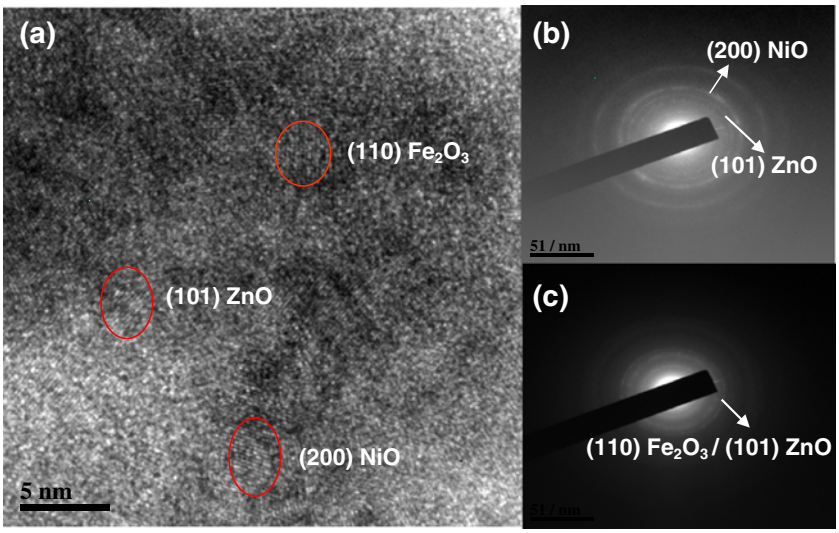

Fig. 5 TEM photographs of particles of cycled electrodes of $(Ni_{0.4}Zn_{0.6})Fe_2O_4$ (second cycle; charged to 3 V) **a** HRTEM lattice image. *Circles* indicate the metal oxides along with Miller indices. **b**, **c** SAED pattern in different regions. Metal oxides along with Miller indices are indicated

$ZnFe_2O_4$ (x=1) performs very well in comparison to the other compositions with varying x and the general trend of the discharge capacity with cycle number, up to 50 cycles (Fig. 4 and Table 2) is in good agreement with the literature data [4, 5, 22]. The second discharge capacity of 1,215 mAh g^{-1} gradually decreases to 900 mAh g^{-1} after 20 cycles and to 835 mAh g^{-1} after 50 cycles (83% of theoretical capacity). The capacity fading between 10 and 50 cycles is 18%. For comparison, Guo et al. [4] observed a reversible capacity of 800–850 mAh g^{-1} between 2 and 50 cycles when the hollow spherical $ZnFe_2O_4$ is cycled in the range 0.005–3 V at a current of 65 mAg^{-1}. Ding et al. [22] observed a second discharge capacity of 970 mAh g^{-1} which gradually degraded to 834 mAh g^{-1} after 50 cycles (14% capacity fading) when the nano-structured $ZnFe_2O_4$ was cycled between 0.01 and 3 V at a current of 116 mAg^{-1}.

Ex situ TEM

The Li-cycling mechanism from the second cycle onwards (after structure destruction after the first-discharge) is through the conversion reaction and Li-alloying–de-alloying of Zn, as per the reversible reactions of Eqs. 4, 5, 6, and 8. They are proposed based on the work of Guo et al. [4], Sharma et al. [5], and the group of Tirado [6, 11–13]. Using

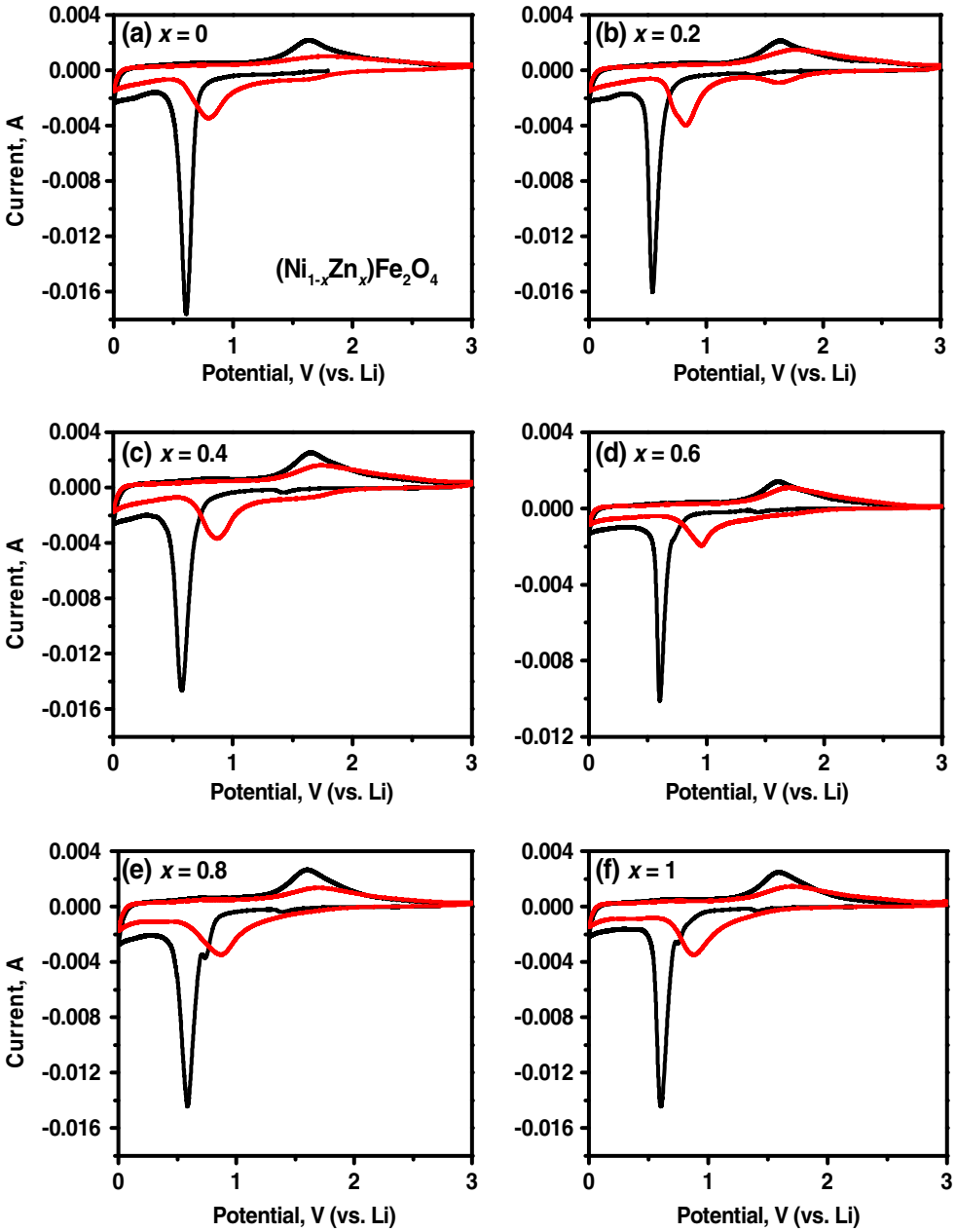

Fig. 6 Cyclic voltammograms of $(Ni_{1-x}Zn_x)Fe_2O_4$. **a** x=0, **b** x=0.2, **c** x=0.4, **d** x=0.6, **e** x=0.8, and **f** x=1.0. Potential window, 0.005–3 V; scan rate, 58 μVs^{-1}. Li metal was the counter and reference electrode. First cycle in *black* color and second cycle in *red* color

HRTEM and SAED patterns, Guo et al. [4] have shown that in $ZnFe_2O_4$, nano-size Fe-metal and Li-Zn alloy particles are formed at the end of first-discharge up to 0.005 V vs. Li. Similarly, nano-size Fe_2O_3 and ZnO particles are formed at the end of first-charge up to 3 V. This is preceded by the de-alloying of (Li–Zn) to form Zn-metal (backward reaction of Eq. 4).On the other hand, Sharma et al. [5] found that nano-size FeO and ZnO particles are formed at the end of first-charge. This discrepancy is possibly due to the sub-micron particle size of $ZnFe_2O_4$ employed by the authors.

Presently, ex situ HRTEM and SAED studies were carried out on the nano-phase, $(Ni_{0.4}Zn_{0.6})Fe_2O_4$ (x=0.6) of the charged electrode after two cycles to identify the oxide phases. The HRTEM lattice image (Fig. 5a) clearly shows the nanocrystalline regions dispersed in Li_2O matrix. As expected, the presence of ZnO, NiO, and Fe_2O_3 is clearly evident from the HRTEM image and SAED pattern (Fig. 5b, c) as the evaluated d values match well with those in the JCPDS cards (ZnO, 89–7102; NiO, 89–7130; Fe_2O_3, 89–8104).

Cyclic voltammetry

The cyclic voltammograms (CV) of the nanocrystalline $(Ni_{1-x}Zn_x)Fe_2O_4$, x=0 to 1, up to six cycles at the slow scan rate of 58 μVs^{-1} between 0.005 and 3.00 V(vs. Li) were recorded. For clarity, CVs of the first two cycles are shown in Fig. 6. It can be seen that the first cathodic scans of all compounds in the CV differ from the subsequent cycles. During first cathodic scan, all the phases showed a high intensity peak at 0.6 (±0.2) V vs. Li. This peak can be attributed to crystal structure destruction due to the reduction of Ni(II), Zn(II), and Fe(III) to the corresponding metal nanoparticles and also the formation of SEI due to the reduction of solvents in the electrolyte (Eqs. 3 and 7). For compositions x=0.8 and 1, a small peak just before the onset of main peak centered at 0.6 V can be ascribed to the Li-intercalation in to the spinel structure before the crystal structure destruction. For the composition x=0.6, the small peak is barely visible due to the smaller content of Zn (Fig. 6d). Compared with the first cycle CV, the original cathodic peak at 0.6 V shifts to ~0.8 V in the second cycle for all x. All other peaks disappear indicating a different Li-cycling mechanism. The cathodic peak located at ~0.8 V is associated to the reversible reductive reaction of ZnO, NiO, and Fe_2O_3 as per Eqs. 5, 6, and 8. As mentioned earlier, due to smaller content of Zn (27 wt.%) in comparison to Fe in $ZnFe_2O_4$ and for the composition with x>0.6, the Li–Zn alloying reaction occurring below 0.35 V is not seen clearly in the CV.

The anodic peak at ~1.6 V was observed in the first charge cycle for all the compositions which is slightly shifted and became broad in the subsequent cycles. The broad peak may include the peaks related to oxidation of Fe, Ni, and Zn nanoparticles. According to literature reports, the oxidation of Fe^0, Ni^0 to Fe^{3+}, Ni^{2+}, respectively occurs at ~1.7 V [14] and that of Zn^0 to Zn^{2+} at ~1.5 V [25]. The area under the peak decreases in the subsequent cycles indicating capacity fading.

Conclusions

Sol–gel auto-combustion method using citric acid as the complexing agent was adopted to prepare nano-phase $(Ni_{1-x}Zn_x)Fe_2O_4$, x=0 to 1. Rietveld-refined XRD data, HRTEM, and SAED show spinel structure with nanoparticles of size range 20–50 nm are formed. Increase in x drives the system from inverse to normal spinel, i.e., a decrease in the degree of inversion and almost Vegard's law behavior for the cubic lattice parameter is observed after Rietveld fitting with positional parameters. Two-phase Li-intercalation reaction (in the voltage 0.9 to 0.8 V) in to the spinel structure is found for the compositions with $x \geq 0.6$, during first-discharge with Li. Galvanostatic cycling studies in the voltage range 0.005–3 V vs. Li at a current of 50 mAg^{-1} show high reversible capacities, 1,065 to 1,215 mAh g^{-1} at the second discharge cycle but continuous decrease in capacity is noted up to 10–15 cycles for all x. The capacity fading between 10 and 50 cycles is ≥56% for x=0, 0.2, and 0.4 whereas it is 52% for x=0.8. For x=0.6 and x=1, the respective values are 40% and 18%, showing a capacity of 570 and 835 (±10) mAh g^{-1} at the end of 50 cycles. Complementary cyclic voltammetry and ex situ TEM data are presented supporting the Li-cycling mechanism involving conversion reactions and Li–Zn alloying–dealloying reaction.

References

1. Yoshio M, Brodd RJ, Kozawa A (eds) (2009) Lithium-ion batteries: science and technologies. Springer, New York
2. Cabana J, Monconduit L, Larcher D, Palacín MR (2010) Adv Mater 22(35):E170–E192
3. Taberna L, Mitra S, Poizot P, Simon P, Tarascon JM (2006) Nat Mater 5(7):567–573
4. Guo X, Lu X, Fang X, Mao Y, Wang Z, Chen L, Xu X, Yang H, Liu Y (2010) Electrochem Commun 12(6):847–850
5. Sharma Y, Sharma N, Subba Rao GV, Chowdari BVR (2008) Electrochim Acta 53(5):2380–2385
6. Lavela P, Tirado JL (2007) J Power Sources 172(1):379–387
7. Kalai Selvan R, Kalaiselvi N, Augustin CO, Doh CH, Sanjeeviraja C (2006) J Power Sources 157(1):522–527
8. Sharma Y, Sharma N, Subba Rao GV, Chowdari BVR (2009) Bull Mater Sci 32(3):295–304
9. Ariyoshi K, Makimura Y, Ohzuku T (2009) In: Ozawa K (ed) Lithium ion rechargeable batteries, vol 2. WILEY-VCH Verlag GmbH & Co. KGaA, Weinheim

10. Chen CJ, Greenblatt M, Waszczak JV (1986) Solid State Ionics 18 & 19:838–846
11. Vidal-Abarca C, Lavela P, Tirado JL (2010) J Phys Chem C 114 (29):12828–12832
12. Alcantara R, Jaraba M, Lavela P, Tirado JL, Jumas JC, Olivier-Fourcade J (2003) Electrochem Commun 5:16–21
13. Lavela P, Kyerematenga NA, Tirado JL (2010) Mater Chem Phys 124(1):102–108
14. Zhao H, Zheng Z, Wong KW, Wang S, Huang B, Li D (2007) Electrochem Commun 9(10):2606–2610
15. Zhao Y, Li J, Ding Y, Guan L (2011) J Mater Chem 21:19101–19105
16. Sharma Y, Sharma N, Subba Rao GV, Chowdari BVR (2007) Adv Funct Mater 17(15):2855–2861
17. Yang Y, Zhao Y, Xiao L, Zhang L (2008) Electrochem Commun 10(8):1117–1120
18. Poizot P, Laruelle S, Grugeon S, Dupont L, Tarascon JM (2001) J Power Sources 97–98:235–239
19. Hankare PP, Sankpal UB, Patil RP, Mulla IS, Sasikala R, Tripathi AK, Garadkar KM (2010) J Alloys Compd 496(1–2):256–260
20. Cherian CT, Reddy MV, Magdaleno T, Sow C-H, Ramanujachary KV, Subba Rao GV, Chowdari BVR (2012) CrystEngComm 14:978–986
21. Shannon RD (1976) Acta Crystallogr Sect A: Found Crystallogr 32(5):751–767
22. Ding Y, Yang Y, Shao H (2011) Electrochim Acta 56(25):9433–9438
23. Wang J, King P, Huggins RA (1986) Solid State Ionics 20(3):185–189
24. Wang H, Pan Q, Cheng Y, Zhao J, Yin G (2009) Electrochim Acta 54(10):2851–2855
25. Deng Y, Zhang Q, Tang S, Zhang L, Deng S, Shi Z, Chen G (2011) Chem Commun 47(24):6828–6830